Green Chemistry

PAPER

View Article Online
View Journal | View Issue

Cite this: *Green Chem.*, 2025, **27**, 4713

Conversion of natural tissues and food waste into aerogels and their application in oleogelation†

Lara Gibowsky, [a,e] Lorenzo De Berardinis,[c] Stella Plazzotta, [c] Erik Manke,[a] Isabella Jung,[a] Daniel Alexander Méndez, [d] Finnja Heidorn,[a] Gesine Liese, [b] Julia Husung,[b] Andreas Liese, [b,e] Pavel Gurikov, [a,f] Irina Smirnova,[a,e] Lara Manzocco[c] and Baldur Schroeter *[a,e]

Received 8th November 2024,
Accepted 26th February 2025

DOI: 10.1039/d4gc05703a

rsc.li/greenchem

In this work, various natural tissues were for the first time directly converted into nanostructured aerogels by utilizing their intrinsic (meso-)porosity. In contrast to common aerogel production, no use of pure biopolymers, their extraction, dissolution, gelation or use of additives (*e.g.* crosslinkers, acids and bases) was necessary. The production process required washing of the wet starting material with water, a solvent exchange with ethanol and drying with supercritical CO_2. The resulting materials exhibited low bulk densities (0.01–0.12 g cm^{-3}), significant specific surface areas (108–446 m^2 g^{-1}) and mesopore volumes (0.3–2.6 cm^3 g^{-1}). Assessment of 20 different tissues including fruit pulp and peel, vegetable pulp, and mushrooms showed the generality of the approach. A broad spectrum of different microstructures was identified, whereas especially textural properties of samples derived from water rich pulp were highly similar to those found in classical biopolymer aerogels, for instance based on pectin or cellulose. Furthermore, the capability of the materials to structure liquid sunflower oil was shown: the produced oleogels exhibited exceptionally high oil uptake (max. 99%) and rheological properties similar to those of solid fats. Results suggest that supercritical drying of tissues (*e.g.* based on food waste) is a suitable approach for their upcycling into value added materials by a complete green and sustainable process. This research also contributes to sustainable development by transforming food waste into valuable aerogels and promoting science education through accessible, open-source STEM resources.

Green foundation

1. Our research enables the sustainable conversion of natural tissues into aerogels without biopolymer extraction or synthetic additives. Unlike conventional sol–gel methods, it eliminates strong acids, bases, and toxic solvents, reducing chemical waste and energy consumption.
2. We directly transform food waste (*e.g.*, fruit peels, vegetable fibers, mushrooms) into nanostructured aerogels using a green process involving water washing, ethanol exchange, and supercritical CO_2 drying. These eco-friendly aerogels feature high surface areas and ~99% oil absorption, making them ideal in application as sustainable oleogels.
3. Optimization could reduce ethanol and CO_2 consumption *via* recovery systems. Low-energy vacuum drying and bio-based solvents could further enhance sustainability. Incorporating enzymatic treatments and expanding the use of agricultural by-products would strengthen the circular economy and broaden applications beyond food and pharmaceuticals.

[a]*Institute of Thermal Separation Processes, Hamburg University of Technology, Eißendorfer Straße 38, 21073 Hamburg, Germany. E-mail: baldur.schroeter@tuhh.de*
[b]*Institute of Technical Biocatalysis, Hamburg University of Technology, Denickestraße 15, 21073 Hamburg, Germany*
[c]*Department of Agricultural, Food, Environmental and Animal Sciences, University of Udine, Via Sondrio 2/A, 33100 Udine, Italy*
[d]*Food Safety and Preservation Department, Institute of Agrochemistry and Food Technology (IATA-CSIC), Valencia, Spain*
[e]*United Nations University Hub on Engineering to Face Climate Change at the Hamburg University of Technology, United Nations University Institute for Water, Environment and Health (UNU-INWEH), Hamburg, Germany*
[f]*aerogel-it GmbH, Albert-Einstein-Str. 1, 49076 Osnabrück, Germany*
† Electronic supplementary information (ESI) available. See DOI: https://doi.org/10.1039/d4gc05703a

1 Introduction

Food loss and waste account for approx. 44% of global waste and around 30% of global food production: according to the United Nations Food Waste Index Report 2024, an estimated 931 million tons of food loss and waste are generated annually worldwide.[1,2] In line with the UN sustainable development goal 12.3, the aim is to reduce this amount by 50% by 2030. To achieve this, both the avoidance and valorization of food waste have become crucial measures in recent years. The latter includes the upcycling of food and agricultural waste, reintegrating both edible and inedible parts (*e.g.* unutilized parts like residual pulp, peels, plant body leftovers) back into the human supply chain, but also its conversion into value added products which exceed the food-sector, for instance natural dyes, membranes, hydrogels and bio-fuels.[2–5] An alternative/supplement to the direct conversion of food waste into high-value products is the extraction of bioactive compounds, including secondary metabolites, phytochemicals, oils, unsaturated fatty acids, and polysaccharides, as well as dietary fibers: such approaches require the development of green, cost-efficient, and selective extraction methods.[3,6] Amongst various processes, supercritical fluid extraction (SFE) utilizing supercritical CO_2 ($scCO_2$) stands out as a widely used and green technique, which is comparably cheap, easily accessible, selective, and generally recognized as safe (GRAS).[7,8]

Non-extractive valorization of food waste involves its direct use as a value added product, *e.g.* as a fertilizer or feed for livestock: hereby dry residues are normally used which contain approximately 65% carbohydrates, 12% crude proteins and a high fiber content of about 13%.[3,9] Depending on the final solid shape (*e.g.* granules, chips, powders) and particular application, various different drying techniques are applied (for instance solar-, freeze-, and vacuum-drying, aeration, biological conversion, spray-, and drum processes).[10] $scCO_2$-drying offers additional opportunities by enabling microbial inactivation and preservation of valuable properties and components.[11–14] Furthermore, $scCO_2$-drying can be used to avoid the occurrence of capillary forces during the drying process, effectively drying the material without causing microstructural damage.[15,16] It is notable that the unique properties of supercritical fluids are utilized in both processes, SFE and $scCO_2$-drying, but with different objectives. However, $scCO_2$-drying of food products is still generally uncommon, particularly with the aim to preserve the intrinsic microstructure: pioneering studies have focused so far mostly on other aspects like microbial and enzymatic inactivation while providing nutrient retention and an increased shelf life as a result of the $scCO_2$-drying process.[12–14] However, in other fields, $scCO_2$-drying is widely used for the fabrication of materials, whose primary value is rooted in their internal microstructure, namely aerogels.[16]

In a simple description, aerogels are highly porous solids (porosity ε of up to 99%) with low densities, whose microstructures offer a significant mesopore content (pore diameter d_{pore} = 2–50 nm) and high mass specific surface areas (S_m) of up to >1000 $m^2\ g^{-1}$.[17,18] Even though no single definition of the term "aerogel" is so far provided in the literature, truly mesoporous aerogels are clearly distinguishable from other porous materials by their microstructural features. In particular, freeze-drying as opposed to supercritical drying leads to so called cryogels, which resemble coarse, solid foams due to their macroporous nature (pore diameter in the micrometer range) and lack therefore the distinguished properties (like a high S_m) of aerogels.[16,19]

This is especially demonstrated by works in which both drying techniques are directly compared.[20,21] In this sense, the numerous works reporting the production of "aerogels" (from food waste and in general) *via* freeze-drying should critically be checked regarding the microstructural properties of the resulting materials (see *e.g.*[22–26]). Aerogels can principally be derived from any material (classically silica, but also various polymers and even metals). Amongst these, biopolymer aerogels show properties like biodegradability, biocompatibility and good viscoelasticity, which are desirable in food and pharma applications.[17,27–29] The production of mesoporous biopolymer aerogels requires generally several steps, whereas the first step is in most cases the extraction and dissolution of a pure biopolymer in an appropriate solvent (Fig. 1).[16] The subsequent build-up of three-dimensional pore networks (hydrogel formation, step 2) is achievable *via* sol–gel conversion: gelation of dissolved biopolymer molecules is hereby inducible *via* different methods (*e.g.* physical, ionic or covalent crosslinking).[16] Follow-up steps are (3) the exchange of water by an organic solvent, in most cases ethanol and (4) removal of the liquid solvent by $scCO_2$-drying, typically carried out at pressures in the range of 100–150 bar and slightly elevated temperatures >35 °C.[30] Even though various biopolymer-to-aerogel routes have been established in recent years[16] (including conversion of agricultural waste[22] and biorefinery approaches[31]), it is crucial to minimize overall production costs of aerogels in order to enhance their competitiveness on the market. Besides optimization of solvent exchange[32,33] and supercritical drying steps,[34–36] the isolation of pure biopolymers from mixtures/composites and their dissolution should also be taken into account as cost driving and sustainability factors in the aerogel production line. For instance, cellulose is a not easily soluble biopolymer and the use of expensive or non-green solvents like aqueous alkali/urea mixtures,[37] ionic liquids[38] or molten salt hydrates[39] is therefore required.[15,40] Alternative approaches based on nanocellulose fibers avoid the sol–gel route and eliminate the dissolution step, but require the extraction of nanocellulose from biomass/cell walls (which is complicated) and demand typically further cost and energy intensive pretreatment, *e.g.* mechanical (such as grinding, separation), chemical, biological or combined methods.[40] In the case of any biopolymer, the use of dissolution and crosslinking agents (like acids, bases, metal salts, *etc.*) increases the requirement for additional washing steps to remove chemical residuals from the pore matrix.[37,41]

Recently, conversion of different orange parts into aerogels (peels, bagasse and pulp) by supercritical drying was

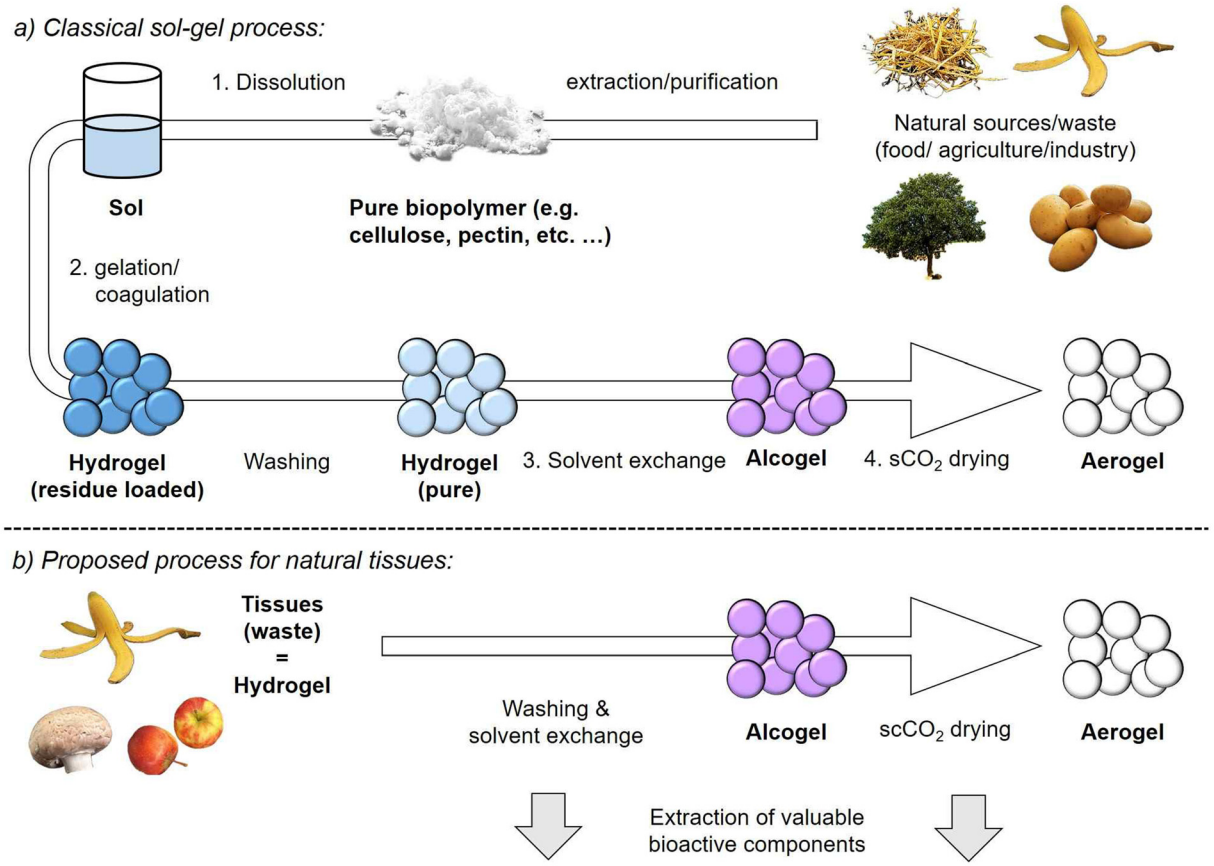

Fig. 1 (a) Processing scheme for production of biopolymer aerogels from single components *via* the sol–gel route. (b) Proposed process for the direct conversion of natural tissues into aerogels.

reported.[42] While this study highlights the possibility to transform a complete fruit-body into biopolymer aerogels, the intrinsic porosity of the orange-tissue was not used, since orange parts were first dried under ambient conditions (leading to mesopore-collapse). The pectin fraction was subsequently extracted and processed *via* the classical sol–gel route to form a porous matrix around non-dissolved orange parts.[42] Generally, a question could be raised: why valuable biopolymers like pectin, cellulose, proteins and others should pass the steps of extraction, dissolution and gelation, rather than being directly converted to aerogels in their unaltered, intrinsically porous and natural tissue-based form. To address this matter, it is necessary to evaluate whether and to which extent supercritically dried natural tissues meet the criteria for being classified as "aerogels", and how they compare to sol–gel-based aerogels in typical applications. So far, only a few pioneering works have dealt with $scCO_2$-drying of natural tissues with respect to the resulting microstructures. Promising results were found for fresh cut salad waste, spent ground coffee and apple pomace tissues, whereas $scCO_2$-dried products demonstrated aerogel-like behavior, *e.g.* low bulk densities, the presence of mesopores and significant specific surface areas (S_m = 112–229 $m^2\ g^{-1}$).[43,44] $ScCO_2$-dried salad waste showed high water and oil sorption capability,[45] indicating the potential use as a bulking agent or as a porous matrix for absorption of liquid, edible oils.

Considering their origin, it seems natural to use such materials in the food-sector: microstructural properties and composition render biopolymer aerogels indeed promising in food related applications, *e.g.* in food packaging or use as encapsulants and smart, functional ingredients.[27,46] Open porosity and high specific surface area allow for quick, capillary force-driven uptake of oil, which is then held in the aerogel matrix *via* surface–oil interactions.[27] This so called templating approach in oleogelation enables accordingly structuring of liquid, edible oils into semi-solid systems (oleogels), which represent a healthier alternative to solid, saturated fats and is *e.g.* applicable as a food ingredient in spreads.[47,48] In previous studies, mesoporous whey- and potato protein isolate based aerogels have already been successfully converted into firm oleogels, showing hereby a high overall oil uptake >75% and sufficient oil holding capacities OHC (OHC up to 96%).[47,49,50] It was found that these performance related criteria are connected to the microstructural properties of the aerogel template (*e.g.* specific surface area, meso- and macropore volumes) and to the polarity differences between oil and aerogel surfaces.[20,27,49,50]

The aim of this work is to propose a new way for food waste valorization by the direct conversion of natural tissues into

biopolymer aerogels *via* $scCO_2$-drying. So far, it has not been shown that a direct tissue-to-aerogel route (which avoids biopolymer and nanofiber isolation as well as sol–gel chemistry) is generally feasible and leads to competitive products. In order to assess the generality of the approach, a screening of twenty different tissues derived from fruit pulp, peels, mushrooms, and vegetables (including roots) is carried out. Samples are categorized based on their microstructure and compared with "conventional" sol–gel based biopolymer aerogels from single components. Finally, the application of the materials as oleogel templates is assessed by testing the capability of selected samples to adsorb edible liquid sunflower oil and to structure it into semi-solid oleogels. This research supports directly several UN Sustainable Development Goals (SDGs) as being a member of the United Nations University Hub at the Hamburg University of Technology.[51] (1) By providing innovative methods to convert food waste into functional materials, advancing SDG 12 (responsible consumption and production) and SDG 9 (sustainable industrialization). (2) By upcycling natural food fabrics, we reduce environmental impact, promote resource efficiency and provide bio-based, sustainable alternatives to synthetic materials. (3) In addition, we address SDG 4 (quality education) through our open-access STEM platform, aerogel.kniffelix.de, which enables educators, students and the public to engage in science-based learning about aerogels, hands-on experimentation and sustainability-oriented innovation.[52,53] This initiative not only advances sustainable technologies, but also empowers future generations to adopt environmentally friendly practices.

2 Materials and methods

2.1 Preparation of supercritically dried tissues

In total, 20 different tissue-based samples from fresh fruits, vegetables, and mushrooms have been prepared (for a complete sample list, see Table S1,† all starting materials were purchased at a local market). In the case of fruits and vegetables, the pulp has been separated from the remaining components like seeds and peels. The mushroom sample was processed without further separation. The desired parts (~500 g) of the samples were subjected to 500 ml distilled water and shredded in a kitchen mixer (Bosch Stand Blender MMB6174S VitaPower). Shredded tissues were then washed in 10 L distilled water at room temperature for 12 h under stirring (overhead stirrer 750 rpm). The water was replaced, and the washing process was repeated three times with fresh distilled water to extract water-soluble components from the tissue-matrix. Subsequently, a direct solvent exchange from water to ethanol was carried out at room temperature, by placing samples in 99.9 wt% ethanol (EtOH, denatured, Carl Roth GmbH & Co. KG). This procedure was repeated with fresh EtOH until a minimum final concentration of 97.0 wt% EtOH inside the samples was reached (controlled by density measurements, Anton Paar, DMA 4500 M). In the case of samples which were later used in oleogelation, an additional wet milling step was applied after the solvent exchange was completed. This was done to achieve small particle sizes in the range of 50–100 μm which are optimal in terms of sensory effects during consumption.[54] The procedure was carried out according to former works,[47,55] using a colloid mill (IKA Magic LAB 1508) and applying a rotational speed of 22 000 rpm and a gap width of 900 μm in the rotor-stator system. All solvent exchanged samples (alcogels) were sealed in filter paper bags and transferred into an autoclave (volume = 3.9 L). Drying with supercritical CO_2 was then performed at a pressure of 120 bar and a temperature of 40 °C under a continuous CO_2 flow (120–140 g min^{-1}) until complete extraction of EtOH was achieved (approx. 3 hours drying time). Samples were collected after slow depressurization (2 bar min^{-1}) of the autoclave and stored in 250 ml vessels sealed with parafilm in a desiccator over calcined silica gel until further use and analysis.

2.2 Characterization of supercritically dried tissues

Low temperature Nitrogen adsorption–desorption physisorption was carried out to investigate the microstructural properties of supercritically dried samples (Nova 3000e Surface Area Analyzer, Quantachrome Instruments, Boynton Beach, USA). Prior to each measurement, the corresponding sample was degassed in a measurement cell under vacuum at 60 °C for at least 6 h. A sample amount of 20–30 mg was used in each run. The Brunauer–Emmett–Teller (BET) method was used in the p/p_0 range of 0.027–0.27 to estimate the mass specific surface area (S_m). The mesopore volume V_{meso} and the mean mesopore diameter ($d_{pore,\ mean}$) were estimated *via* the Barrett–Joyner–Halenda (BJH) method. Standard errors for determination of S_m and V_{meso} were estimated based on a threefold determination ($S_m \pm 5\ m^2\ g^{-1}$, $V_{meso} \pm 0.14\ cm^3\ g^{-1}$). The skeletal density ρ_S was determined *via* helium pycnometry (Multivolume Micromeritics AccuPyc II 1340, Norcross; GA USA) at room temperature. A 4-fold determination was performed for each sample. For estimation of the bulk density, a defined volume of sample (11.5 cm^3) was filled in a container without tapping and the weight was determined on an analytical scale (Excellence Plus XP, Mettler Toledo). The solid bulk densities ρ_B were calculated as the ratio of the sample mass (m) and the sample volume (V) according to eqn (1):

$$\rho_B\,[g\,cm^{-3}] = \frac{m\,[g]}{V\,[cm^3]} \quad (1)$$

The porosity ε was estimated based on bulk- and skeletal densities:

$$\varepsilon\,[\%] = \left(1 - \frac{\rho_B\,[g\,cm^{-3}]}{\rho_s\,[g\,cm^{-3}]}\right) \times 100\% \quad (2)$$

The inner pore structure of samples was characterized *via* scanning electron microscopy (SEM, Zeiss Supra VP55, Jena, Germany). Substrates were sputtered with a conductive, thin (approx. 6 nm) layer of gold (Sputter Coater SCD 050, BAL-TEC) prior to analysis. Measurements were carried out under high vacuum at an accelerating voltage of 3.00 kV, a

working distance of 3.3–4.5 mm using an in-lens detector. Images of substrate powders were taken in a fotobox. The brightness and contrast of the SEM and photographic images were optimized using PowerPoint 2016. The neutral sugar and uronic acid composition of supercritically dried samples was analyzed following a modified procedure after acidic methanolysis.[56] In brief, 1 mg of each sample was first freeze-dried and then subjected to methanolysis by incubation with 1 mL of 2 M HCl in anhydrous methanol at 100 °C for 5 hours. The reaction was then neutralized using pyridine, followed by drying under a stream of air. To further hydrolyze the samples, they were treated with 2 M trifluoroacetic acid at 100 °C for one hour. After repeated drying under an air stream, the samples were resuspended in MilliQ water, filtered (0.22 μm pore size), and injected for analysis. Monosaccharide analysis was carried out using high-performance anion exchange chromatography coupled with pulsed amperometric detection (HPAEC-PAD) on an ICS-6000 system (Thermo Fisher Scientific) fitted with a CarboPac PA1 column (4 × 250 mm, Dionex). Calibration was performed using control samples with known concentrations of monosaccharides, including glucose, fucose, rhamnose, galactose, arabinose, xylose, mannose, galacturonic acid, and glucuronic acid (Merck, Germany). The cellulose content was estimated as the difference of glucose between methanolysis and Saeman hydrolysis.[57] In brief, 1 mg of each sample previously freeze dried was incubated with 0.125 mL of sulfuric acid for 3 hours at room temperature, then 1.375 mL of milliQ water was added and the samples were sealed and heated for 3 hours at 100 °C. The sample was filtered and diluted 1 : 10 with milliQ water, and then injected using the same equipment of the methanolysis method described previously. Calibration was performed using control cellulose with known concentrations (Merck, Germany). The protein content was quantified by the Dumas combustion method, employing a nitrogen conversion factor of 6.25, in accordance with ISO/TS 16634–2 (2016). All composition analyses were carried out in triplicate. The thermal stability was determined *via* thermogravimetric analysis (Linseis TGA PT 1600). An amount of 20–40 mg of sample was placed in an aluminum oxide crucible, heated with a heating rate of 10 °C min^{-1} to a final temperature of 850 °C under an oxidized atmosphere, followed by a dwelling phase of 120 min. A single bounce diamond ATR insert (MIRacle, Pike Technologies) and a liquid-cooled MCT detector were utilized for obtaining the ATR MIR spectra using a Vertex 70 spectrometer (Bruker Optik GmbH, Ettlingen, Germany). The Vertex 70 spectrometer was purged with dry and carbon dioxide-free air. The spectra were recorded from 4000 cm^{-1} to 600 cm^{-1} with 64 scans per spectrum using the OPUS 7.0 software package (Bruker Optik GmbH, Ettlingen, Germany).

2.3 Oleogel preparation and characterization

Oleogels were prepared by gradually adding sunflower oil (purchased in a local market) to an amount of 0.2 g aerogel, starting with an aerogel-oil weight ratio of 1 : 5. After each addition of oil, the sample was manually mixed, and the appearance was evaluated. Images were obtained after each oil addition using an image acquisition chamber (Immagini & Computer, Bareggio, Italy) equipped with a digital camera (EOS 550D, Canon, Milano, Italy).

The sample was placed on a spatula and positioned approx. 50 cm in front of the camera, with a black cardboard backdrop serving as the background. Light was provided by four 100 W photographic floodlights to optimize the pictures regarding shadow and gloss.

Viscoelastic properties (G' and G'' moduli, and $\tan\delta$) were determined with a Rheometer RS6000 (Thermo Scientific RheoStress, Haake, Germany) equipped with a Peltier system for temperature control. All measurements were performed with a parallel plate geometry at 20 ± 0.5 °C and a gap width of 2 mm. First, the amplitude sweep test was carried out with increasing stresses from 1 to 6000 Pa at 1 Hz frequency to identify the linear viscoelastic region (LVR) of all oleogel samples. Afterward, the frequency sweep test was performed in duplicate at a stress of 10 Pa for all samples, which was determined in the LVR, and an increasing frequency of 0.1 to 15 Hz.

For confocal laser scanning microscopic measurements, oleogel samples were first stained with a 0.001% oil solution of Nile red and a 0.001% ethanolic solution of Fluorescent Brightener 28 (Sigma Aldrich, Milan, Italy), used to stain oil and polysaccharides, respectively. After staining, the samples were placed on a microscope slide, covered with a cover slide, and observed by using a confocal laser scanning microscope at 25 times magnification (Leica TCS SP8 X confocal system, Leica Microsystems, Wetzlar, Germany). Images were imported in tif.format using the software LasX 3.5.5 (Leica Microsystems, Wetzlar, Germany).

The oil holding capacity (OHC) was determined according to previous works.[49] Eppendorf tubes were first weighed empty and then filled with approx. 0.5 g of the respective sample. Subsequently, samples were subjected to centrifugation (15 min at 15 000*g* and 4 °C) (Mikro 120, Hettich Zentrifugen, Andreas Hettich GmbH and Co, Tuttlingen, Germany). After centrifugation, the released oil was removed, and the tubes were weighed again. The OHC of all oleogel samples was calculated according to eqn (3):

$$\mathrm{OHC}\,[\%] = \frac{\text{total oil in sample [g]} - \text{oil relased during centrifugation [g]}}{\text{Total oil in sample [g]}} \times 100\% \quad (3)$$

All measurements were carried out in triplicate.

3 Results & discussion

To explore whether naturally grown tissues can be generally converted into aerogel-like materials, a screening of 20 different tissues, including pulps and peels sourced from fruits, vegetables, and mushrooms, was conducted. The names of supercritically dried samples correspond in the following discussion directly to the educts used in the production. If not

further specified, samples were produced from the pulp; peel-based samples are pointed out in the sample name. In the first part of this study, different physical and textural properties of the dry products are described; in the second part, the applicability of selected samples as oil structuring templates for oleogelation is assessed.

3.1 Properties of samples dried with supercritical CO_2

Processing of natural tissues *via* shredding, washing, solvent exchange and subsequent supercritical drying yielded light weight, fine and odorless powders (Fig. 2). With some exceptions (plum, apple, mushroom, strawberry), colorless products were obtained, showing that pigments such as carotenoids were in most cases completely removed during solvent exchange and supercritical drying steps. The banana peel sample showed a quick color change after transfer into ethanol for solvent exchange due to enzymatic browning,[58] and the coloration was preserved throughout the process (Fig. 2). Other non-polar components (*e.g.* chlorophylls,[59] phytochemicals like polyphenols,[60] fatty acids,[61] and essential oils[62]) are easily dissolvable in supercritical CO_2: therefore their extraction during the supercritical drying (with a high and continuous CO_2-flow) is anticipated.[43] A detailed composition analysis revealed as expected that dry samples were mainly composed of (poly-)saccharides and proteins (for a detailed single component overview for each sample, we refer to Table S2†). While component ratios varied to some extent in between samples of different origin (Table S2†), the average compositions represented typical vegetable/fruit cell wall fractions, with pectin being the main component (~55 wt%), followed by cellulose (~20 wt%), proteins (13 wt%), monosaccharides/sugar acids (~11 wt%) and other components which included most likely fructose, hemicellulose and lignin (overall ~11 wt%).[63,64] As single exception, the mushroom sample (proteins ~43 wt% and chitin ~33 wt%) was not included in the calculation of the aforementioned averaged values. The overall significant monosaccharide fraction found in most samples indicated that some residual monosaccharides remained in the tissue matrix after washing and solvent exchange steps. Alternatively, these fractions could also be breakdown products of various biopolymers, which were obtained during the pre-processing (acidic methanolysis) of samples for the composition analysis. The biopolymer decomposition behaviour might – however – vary throughout the samples: for instance the amorphous regions of cellulose are more accessible and can therefore be broken down into glucose monomers more easily and quickly during acidic hydrolysis, whereas the crystalline regions require harsher conditions for degradation. Furthermore, also hemicelluloses such as xyloglucans and glucomannans contain glucose units that can be released under certain acidic hydrolysis conditions.[65] All identified biopolymer fractions belong to the most common starting materials in biopolymer aerogel production, with cellulose and pectin making up alone for a significant part in all works.[16] Skeletal densities of samples varied slightly (average $\rho_s = 1.73 \pm 0.33$ g cm^{-3}) (Table S1†) and fell in most cases within the usual range reported for the main components.[15,19] Additional FT-IR spectroscopic analysis was performed on all samples, which were subsequently used for oil structuring. The spectra of all samples were largely similar,

Fig. 2 Images of powders obtained after solvent exchange and sCO_2-drying of various natural tissues. Respective sample names are given in the individual images.

with the exception of the mushroom based tissue. Although the resulting spectra represented the mixed (partly overlapping) signals of all components, specific bands corresponding to the main biopolymeric fractions (pectin, cellulose, and chitin in the case of the mushroom sample) were clearly identifiable. For a more detailed interpretation of the spectra, we refer to the description in the ESI and to Fig. S1.† Special attention was given to determine the degree of esterification of the pectin fraction, as this is a crucial factor influencing pectin behavior within cell walls, its gelation properties, hydrogen bonding capability and its interaction with oil.[66] The degree of pectin methoxylation (%DM) was estimated based on the areas of bands at ~1740 cm^{-1} (A_{1740}) and at ~1600–1630 cm^{-1} (A_{1630}) according to eqn (4).[67,68]

$$\%\mathrm{DM} = \frac{A_{1740}}{A_{1740} + A_{1630}} \times 100\% \quad (4)$$

Pectins present in the variety of samples in this work were expected to show pronounced differences at the structural and molecular levels, which could result in different chemical stabilities and decomposition behaviors.[69] Nonetheless, all samples fell within the range of low-methoxyl (LM) pectins, with a %DM of approximately 20% for pectins in banana peel, kiwi, and nectarine and around 40% in those from orange pulp, orange peel, and radish samples. LM pectins are prone to crosslinking in the presence of divalent ions (*e.g.*, Ca^{2+}), generally soluble in water at pH 7 (in the absence of ions) and their dissolution behaviour is generally sensitive to various conditions during the washing step (beyond pH, *e.g.* also temperature and the presence of ions and other biopolymers). While the washing conditions (pH-neutral, demineralized water, 20 °C, ion-free) used in this work were generally suitable for dissolving LM pectin, our results showed that the final products still contained significant amounts. This could be due to a variety of factors, as pectins can interact in complex ways within multi-component food systems, which might affect their dissolution behavior. Consequently, a more in-depth understanding of each individual system would be required to fully explain the particular pectin dissolution behavior in each case. Regarding their use as food ingredients, LM pectins are useful for low-calorie or sugar-free products and are, for instance, used in low-fat desserts, reduced-calorie jams, puddings, and plant-based gelatin alternatives. In terms of the given use case (oleogelation) weaker interactions with oil, compared to high %DM (>50%) pectins, are expected, due to the increased number of free carboxyl groups which lead to a higher hydrophilicity. Insights into the thermal stability of samples were provided *via* TGA analysis under an oxidizing atmosphere. As anticipated, the individual decomposition patterns exhibited some variation (Fig. S2a†). However, all curves followed a general trend typical of (bio)polymer decomposition (Fig. S2b†).[70] Three distinct phases were identified: (1) loss of residual water (dehydration), causing a slight mass decrease (T = 20–100 °C), (2) decomposition of organic materials (*e.g.*, cellulose, chitin, pectin, proteins), leading to significant mass loss (T = 100–465 °C). This phase includes decomposition mechanisms like main- and side-chain scission, elimination, depolymerization, cyclation and crosslinking.[70] While the most pronounced biopolymer decomposition occurred at temperatures above 165 °C, slow decomposition occurred already at lower temperatures. (3) Continued decomposition of the remaining organic matter under formation of inorganic residues (*e.g.* ash), with stable and lower mass loss (T = 465–850 °C).

In order to assess the question, if samples can be classified as aerogels, the presence of internal mesoporosity was evaluated *via* nitrogen physisorption and SEM measurements. Physisorption data were evaluated for 17 out of 20 samples (general criteria: R^2 of the BET-plot ≥0.999, positive C constants and regular isotherms, see Table S1 and Fig. S3 S4†). Significant specific surface areas in the range of S_m = 108–354 $m^2\ g^{-1}$ were estimated for all samples (Table 1). Hereby, lower values <230 $m^2\ g^{-1}$ were in the same range of those previously reported for supercritically dried salad leaf, apple and coffee tissues, whereas the majority of samples exhibited higher specific surface areas.[43,44] Adsorption–desorption isotherms of the corresponding measurements showed in all cases a hysteresis (type IV), which is related to mesoporous adsorbents (for normalized isotherms averaged by shape see Fig. 3a, for single sample isotherms we refer to Fig. S3†).[71–73]

While the shape of the hysteresis loops did not necessarily match the idealized IUPAC classifications (H1–H6 shape), three distinct isotherm shapes were identified (Fig. 3a), which suggested the presence of separate sample categories with different microstructural properties. Differences at the microstructural level were evaluated in detail by plotting the normalized, cumulative internal surface areas against the mesopore diameter (Fig. 3b). This allowed us to assess up to which extent mesopores of different size-regimes contributed to the overall specific surface area of a given sample (Table 1).

Based on the results, samples were assignable to three distinct categories which represent different microstructures. Samples with small mesopores ($d_{pore} \leq 6.5$ nm) contributing to a large extent to the overall specific surface area (≥60%) were assigned to category 1. Larger mesopores (d_{pore} = 10–50 nm) presented only a small amount of surface area in these cases. This picture was reversed in category 3 samples, where large mesopores contributed most significantly to S_m (up to 83%) and small mesopores in the range of d_{pore} = 6.5–10 nm accounted for max. 30% of the S_m (with some exceptions where these pores were almost negligible, *e.g.* in kiwi and nectarine samples). Category 2 samples showed a significant contribution of all mesopore size-regimes to the S_m, with the slightly highest contribution of the smallest mesopores on average. The aforementioned relations consequently also reflected in the shapes of the corresponding pore size distributions (PSDs) (for normalized PSDs averaged by category see Fig. 3c, single PSDs are shown in ESI, Fig. S5†). Category 1 samples contained mainly mesopores with diameters below 18 nm ($d_{pore,mean}$ ~ 6–10 nm, Table S1†). The provided pore volume increased towards lower mesopore diameters and the presence of even smaller pores (d_{pore} < 4 nm) with sizes below

Table 1 Microstructural properties of supercritically dried, naturally grown tissues and their categorization, based on the contribution of different sized pores to the overall specific surface area S_m

		Sample	S_m [b] overall [$m^2\ g^{-1}$]	V_{meso} [c] overall [$cm^3\ g^{-1}$]	Ratio S_m [a] (≤6.5 nm) [%]	Ratio S_m [a] (6.5–10 nm) [%]	Ratio S_m [a] (10–50 nm) [%]
Sample category	1	Radish	328	0.65	61	30	9
		Apple	202	0.55	63	30	7
		Bell pepper	190	0.31	63	31	6
		Cucumber	238	0.59	60	30	10
		Carrot	125	0.27	62	26	12
	2	Mushroom	281	0.78	43	31	26
		Banana peel	240	0.43	53	29	18
		Pear	168	0.53	48	37	15
		Plum	259	0.93	47	26	27
		Tomato	251	0.74	42	28	30
		Orange peel	285	1.15	36	37	27
		Onion	108	0.30	53	27	20
	3	Kiwi	354	2.56	3	14	83
		Orange	322	1.36	26	40	34
		Honey Pom.	305	1.25	30	39	31
		Strawberry	277	0.94	25	38	37
		Nectarine	248	1.34	9	24	67

[a] Contribution of pores in the given range of pore diameters (nm) to the overall specific surface area in %. [b] Standard error of method ± 5 $m^2\ g^{-1}$. [c] Standard error of method ± 0.14 $cm^3\ g^{-1}$.

the detection limit of the BJH-method is proposed. PSDs of category 2 samples showed in addition to a narrow peak with a maximum at $d_{pore} \sim 10$ nm a broad flank, which suggested the presence of various sized, larger pores with pore diameters $d_{pore} \geq 20$ nm up to the range of small macropores. Category 3 samples exhibited mesopore size distributions which covered the whole mesoporous range with the mean pore diameter falling in the range of medium sized mesopores ($d_{pore,mean} \sim$ 18–30 nm, Table S1†). The corresponding isotherms showed H3-shaped hysteresis loops with a steep increase towards higher p/p_0 values (Fig. 3a and Fig. S3†), which is consistent with the additional presence of macropores.[71] Such isotherms/PSDs are also typical of various sol–gel based biopolymer aerogels with fibrous, multiscale pore networks as *e.g.* reported in recent works on pectins,[73–75] cellulose[41,76] or various proteins[47,77] and pointed towards a high similarity between nanostructures of many "classical" biopolymer aerogels and category 3 samples. Samples of all different categories showed an increasing specific surface area, as the mesopore volume was higher: the overall mesopore volume follows the trend $V_{meso,\ category\ 1} < V_{meso,\ category\ 2} < V_{meso,\ category\ 3}$, whereas values were generally in the typical range reported for biopolymer aerogels (Fig. 3d).[15] It is notable that the relationship between V_{meso} and S_m varied in between samples of different categories. While variation of V_{meso} was not as large throughout category 1 samples, even a slight increase in V_{meso} resulted in a significant increase of the S_m. This is because these samples presented mainly small mesopores, which provided a comparably high surface to volume ratio. For instance, the radish sample showed a high S_m equal to the range of category 3 samples, even though it presented a significantly smaller mesopore volume in comparison. With increasing presence of larger mesopores (and decreasing contribution of smaller ones), more mesopore volume was required to create additional S_m, which was reflected by the trend for category 3 samples (larger variation of V_{meso}, narrow range of S_m). More insights into different microstructures were available by taking results obtained *via* scanning electron microscopy (SEM) into account. In the following, we discuss results with respect to the overall organization of plant tissues and with special emphasis on the question, which parts of the samples are mainly contributing to the mesoporous structure. Due to the diversity of samples and the corresponding cellular and microstructural features, we emphasize however, that the discussion in this study is limited to most fundamental aspects. In general, plant cells can contain various different types of porous tissue: for instance, fruit cells are separated by thin, rather unlignified and nanostructured cell walls which contain pectin/cellulose nanofibers in their subunits (primary and secondary cell walls).[64] These fibers stabilize the cell wall by creating pore networks composed of heterogeneous and variably branched/entangled micro- to nanofibrils, whereas the biopolymer chain length can vary widely in a range from a few tenths of up to several thousand nanometers.[78] Cytoplasmic bridges (plasmodesmata) of various sizes form channels through these walls and enable mass transport (*e.g.* water, nutrients, other materials) between individual cells.[64,79] While the initial definition of these bridges has changed with the development of advanced detection techniques, dimensions and accurate determination of the plasmodesmata size are currently still under discussion: generally, plant biologists acknowledge plasmodesmata nowadays as nanoscaled pores.[79] In the SEM images of lower magnification (250–5000×, Fig. 4 and Fig. S6† for all other tissue-based samples of the screening) cells with sizes of ~20–100 μm were indeed visible in most samples (exceptions: peel & mushroom samples). Folding/deformation of cell walls occurred in many cases; this might be a result of diffusive forces which occurred during

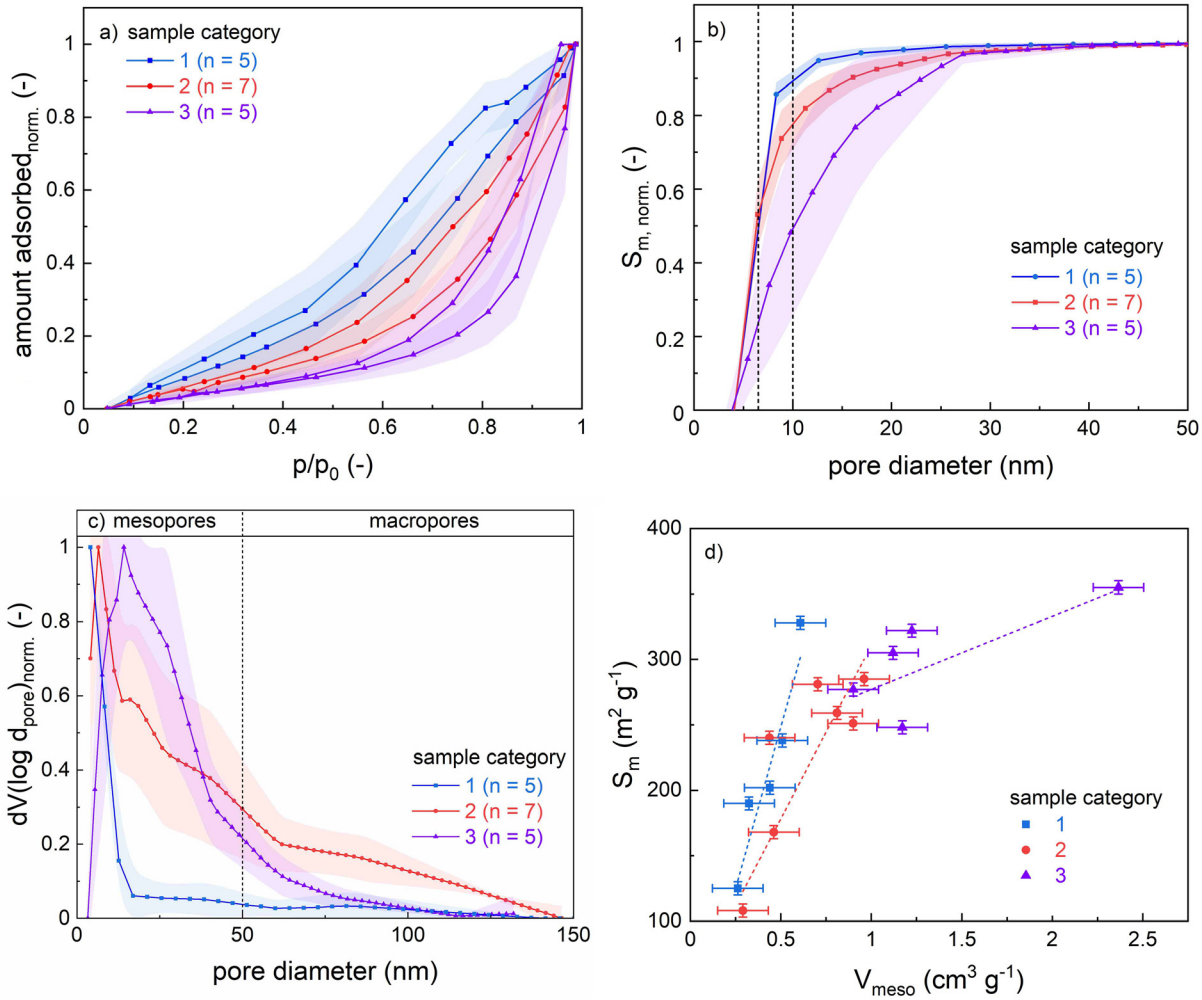

Fig. 3 (a) Normalized nitrogen adsorption–desorption isotherms, averaged by sample category (see Table 1). (b) Normalized cumulative specific surface area plotted against the pore diameter. (c) Normalized pore size distributions, estimated *via* the BJH method. Lines in (a)–(c) are drawn to guide the eye, hatched areas represent the standard deviation of the average and *n* equals the number of samples taken into account. (d) Relationship between mesopore volume and specific surface area for samples of different categories. Error bars represent the absolute error of the methods. Linear trend lines are drawn to guide the eye.

processing (liquids/CO_2 entering and leaving the inner cell body) or caused by the occurrence of mechanical stress during grinding steps.

The stability of the cellular-structure depended on the individual tissue and should generally also be influenced by several, source-related factors, such as the status of the ripening process, the particular microstructure and thickness of the cell wall and the cell size.[64] The flesh of softer fruits (*e.g.* kiwi and orange) consists often of looser tissue with larger intercellular spaces which leads to higher flexibility in contrast to the smaller and denser cell structures of harder fruits and vegetables (*e.g.* radish and carrot, Fig. 4 and Fig. S6†). Consequently, intact/non-deformed cells were not visible in the SEM images of comparably soft category 3 samples (Fig. 4a and Fig. S6†). Images obtained at higher magnifications (50 000–150 000×) were used to identify the most representative mesopore structures, which contributed to V_{meso} and S_m. Hereby, clear differences between mesopore structures across sample categories 1–3 were detected. In category 1 samples, small mesopores were homogenously distributed throughout the cell walls (Fig. 4g and Fig. S6†). In this case, SEM imaging was limited to the outer cell-wall surface and no other mesopores *e.g.* in intercellular spaces or fibrils were determined. No macropores were visible throughout category 1 samples, which is consistent with the N_2-isotherm shape, showing a rather gradual increase in the amount of absorbed nitrogen in the higher p/p_0-range. The small size of pores and the narrow range of the PSD distribution indicated that the mesoporous volume in category 1 samples was partly provided by confined, organized structures. These could include, for example, internal plasmodesmal channels in the cell walls or subunits (*e.g.* the desmotubule, presumed transport channels, cytosolic sleeves), whose dimensions have been reported to be within the range of pore sizes estimated *via* the BJH method.[79,80]

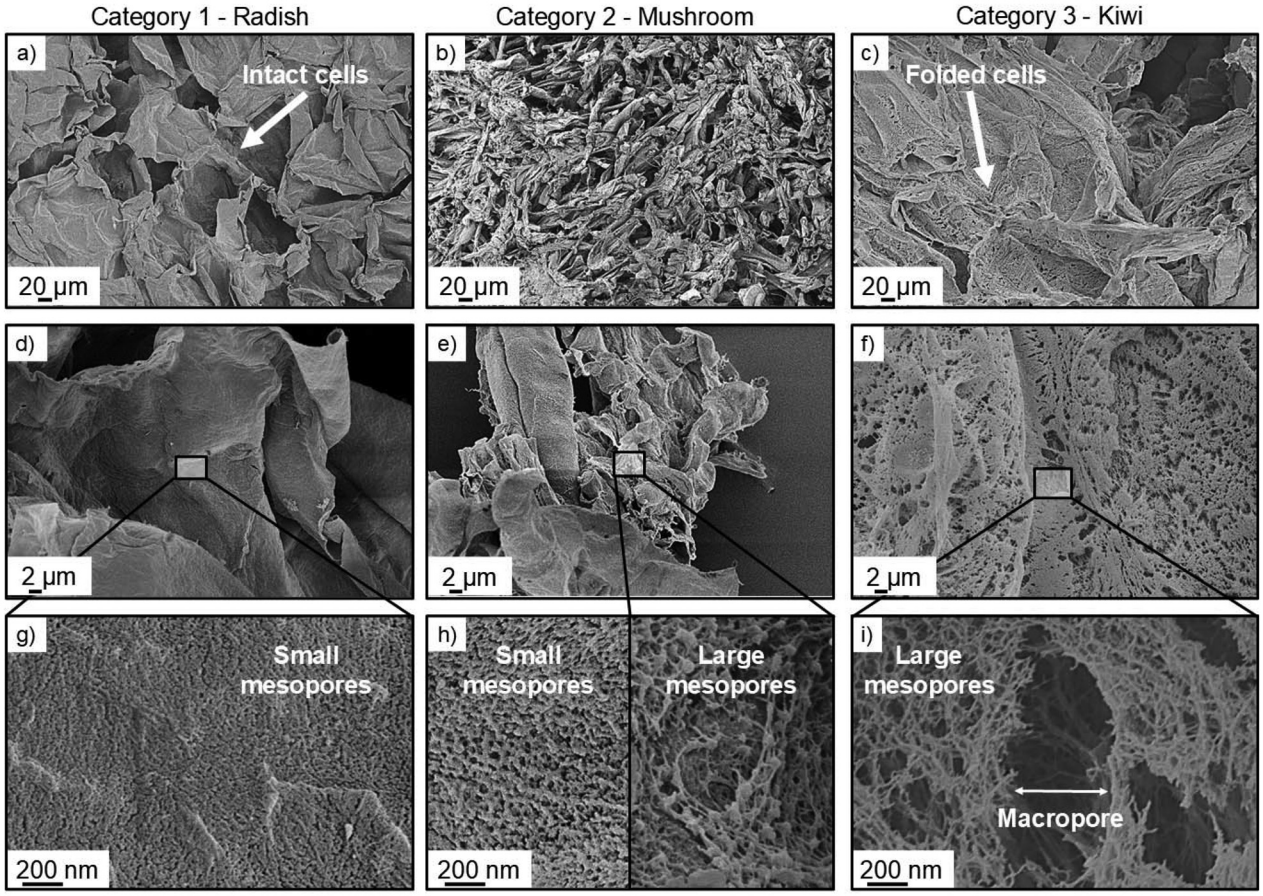

Fig. 4 SEM images of selected samples (radish, mushroom, and kiwi) from different sample categories obtained at different magnifications: (a)–(c) 250×),(d)–(f) 5000×, (g)–(i) 150 000×.

With respect to the overall low volume of such channels, it is nevertheless not clear to which extent they could have possibly contributed to the overall surface area. In contrast, fibrillar and multiscale pore networks with nanometer sized fibers were visible in samples categorized as type 3 (Fig. 4i, 5d–f and Fig. S6†). These fibrillar pore networks were most likely part of the diverse pectin- and cellulose based fibrous cell wall fractions and contained both mesopores of various sizes as well as small macropores in the range of pore diameters from several hundred nanometers of up to a few micrometers. Noteworthy is the high similarity of these microstructures with those of common sol–gel based biopolymer aerogels. Pectin aerogels with comparable macro- to mesoporous networks are *e.g.* producible from apple-, citrus- and watermelon extracted pectin *via* calcium-ion induced and physical crosslinking.[56,75,81,82]

In the case of cellulose aerogels, comparable pore structures are for instance obtainable from microcrystalline cellulose using different cellulose-solvents (*e.g.* NaOH/water, $ZnCl_2$/water, $Ca(SCN)_2$/water, ionic liquids).[20,39,40] An exemplary, direct comparison between various category 3 samples produced in this work and pectin aerogels obtained from citrus extracted pectin is provided in Fig. 5. While the morphology and density of the pore network can be controlled by the amount of dissolved pectin or by the presence of cations in the sol–gel process (see Fig. 5a–c), such kind of control is reduced in the case of tissue-based samples, where the particular morphology depends also on the inherent microstructure of the used tissue (see Fig. 5d–f). Presented examples highlight although the huge variety of mesopore-morphologies present within samples of category 3 in this work. Category 2 samples were generally highly inhomogeneous and included the fungal as well as peel samples, which were differently organized at the cellular level as compared to fruit and vegetable pulp. Besides cell wall residues, small mesopores (equal to category 1) and fibrillar pore networks (equal to category 3) were both visible (Fig. 4b and Fig. S6†). Nitrogen physisorption data indicated that both types of pores contributed in these cases significantly to the overall mesoporous texture (see Fig. 3c). With respect to the overall inhomogeneity of samples (as compared to "pure" aerogels), it is to be mentioned that high resolution SEM imaging of pore structures provided only qualitative insights of selected sample areas. Particularly category 2 and 3 samples contained in many cases also larger nano- (diameter of a few hundred nm) and microfibers or other amorphous parts.

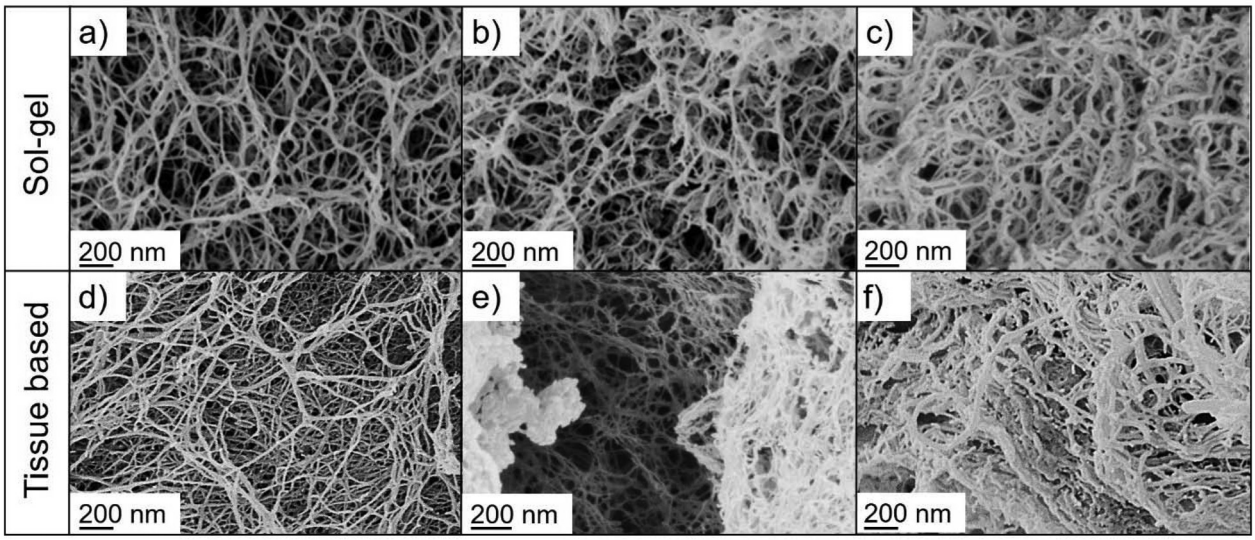

Fig. 5 Pore structures of calcium-ion crosslinked, pectin aerogels produced *via* the sol route (top, Reprinted from[81] with permission from Elsevier, Copyright 2018) and various tissue based samples produced in this work (bottom). Sol–gel based samples were produced with different pectin-contents in the sol: (a) 2 wt%, (b) 4 wt%, and (c) 6 wt%. Represented pore structures from tissue-based samples are: (d) nectarine (e) strawberry and (f) orange.

Overall, our results suggest that the amount of free accessible nanofibrous structures was the largest in the pulp of relatively soft and aqueous fruit bodies, leading on average to higher mesopore volumes and specific surface areas. It is however important to note the composite nature of samples from all categories, with amorphous components being present alongside open-mesoporous, and nanostructured networks. Given the differences between natural tissue-based samples and "sol–gel" based biopolymer aerogels, it is interesting to compare their typical characteristics, such as density and specific surface area (Fig. 6). Parameters were compared with recent works (2008–2023) on aerogels from single components (pectin, cellulose and proteins), which represent ~75% of the composition in tissue-based samples. Studies in which freeze-drying was used as a drying-technique were not included, due to the microstructural differences between cryogels and aerogels. A comparison of the densities (Fig. 6a) highlights the overall light-weight nature of tissue-based samples with bulk densities ranging from ~0.01–0.12 g cm^{-3} (Table S3†). While this points towards a high porosity ≥97% of the powdered samples, we emphasize that ρ_b is a rough estimate for the internal pores. Since the bulk density was calcu-

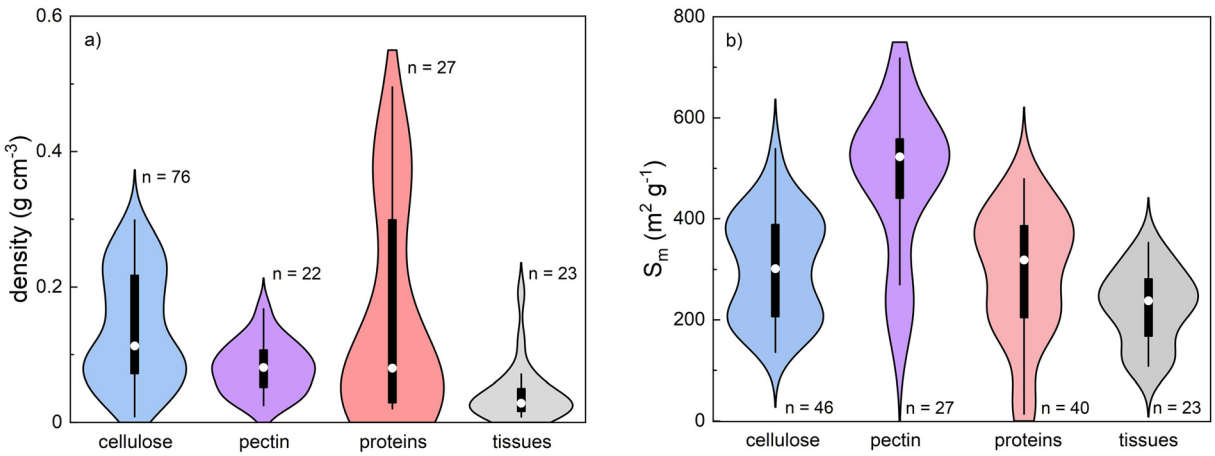

Fig. 6 Comparison of densities (a) and specific surface areas (b) of supercritically dried natural tissues with cellulose, pectin and protein aerogels obtained *via* sol–gel processing of pure biopolymers. The category "tissues" includes combined results from this work as well as available data from former reports.[41,42] The violin plots represent the density of the data along the *y*-axis, the width of the plot represents the frequency density for different values. The black box shows the range between the 1st quartile (25th percentile) and the 3rd quartile (75th percentile). Whiskers represent the range of 1.5 IQR; the white dot corresponds to the median. *n* = number of samples taken into account. All references are listed in Table S3.†

lated from the non-compressed bed of irregular particles ε encompassed both the internal porosity of particles as well as interparticle voids. Because compared works include studies on different aerogel shapes (*e.g.* also monoliths), such interparticle voids were not necessarily present in these cases (leading to higher median values of the density). In the case of S_m, the median of tissue-based samples falls within the same order of magnitude with compared works (Fig. 6b): the overall accessible surface areas in the sol–gel route are nonetheless principally higher due to the homogeneous nature of the samples. In summary, tissue-based samples fulfill the key criteria for materials to be assigned as "aerogels": namely high porosities, low densities, the presence of a significant specific surface area >100 $m^2\ g^{-1}$ and open, three-dimensional mesoporous solid networks.[18,31,40] Differences in tissue-based samples as compared to "sol–gel" based aerogels lie in their heterogeneous nature, leading to a composite-like character. Our results suggest that $scCO_2$-dried natural tissues are principally applicable in many directions, where low densities, a high specific surface area and the presence of mesoporosity play a role. This accounts for leftover pulp and peels as well and highlights the potential use of food waste (*e.g.* generated in juice, jam and essential oil production or in processing for ready meals) as a mesoporous matrix.

3.2 Optimization and ageing

From an application point of view, it is important to evaluate how long food waste can be stored before being converted to an aerogel without compromising the resulting microstructure and composition. A showcase experiment was carried out with orange leftovers, which were directly obtained as a kitchen waste mixture (peel and pulp) after juice production in a fruit press. The samples were stored under ambient conditions (~20 °C) under open air for different times (up to three weeks), prior to further processing. As compared to samples described in section 3.1, significantly less sample (50 g) was used in relation to water during the washing process. This was done in order to (1) ensure the complete removal of monosaccharidic fractions or decomposition products being formed during storage; (2) evaluate if intensified washing influences the final aerogel properties.

In the case of the fresh sample, a significantly increased max. S_m of 446 $m^2\ g^{-1}$ was found (Fig. 7a), which is most likely attributed to the intensified washing. This value exceeds so far reported values for tissue-based samples (compare Table 1 and former studies[43,44]) and is competitive to many sol–gel/nanofiber based aerogels. No pronounced changes of S_m, V_{meso}, and pore size distributions were determined for samples produced after different storage times, and aerogel properties were still obtained after three weeks (Fig. 7). This result showed that no significant evaporative drying of liquid fractions in the inner pores occurred in the investigated time frame. Minor differences between samples were probably related to (1) slight variations in the peel to pulp ratio of individual samples, which was not exactly controlled; (2) changes induced by microbiological/enzymatic conversion, particularly of the pectin fraction. During enzymatic degradation, pectins are broken down by pectinases, leading to depolymerization, solubilization and de-esterification by pectin methylesterases, reducing its %DM. While a corresponding decrease of the % DM over time was expected, our results showed a different trend. Only slight changes in the %DM occurred up to one week storage time and a severe decrease was observed after two weeks (Fig. 7b, for the corresponding IR spectra we refer to Fig. S7†). This was consistent with significant browning of the sample, which occurred after one week (Fig. 7a) and indicated the presence of oxidized phenols (*e.g.*, through polyphenol oxidases) and/or degradation products from pectin. However,

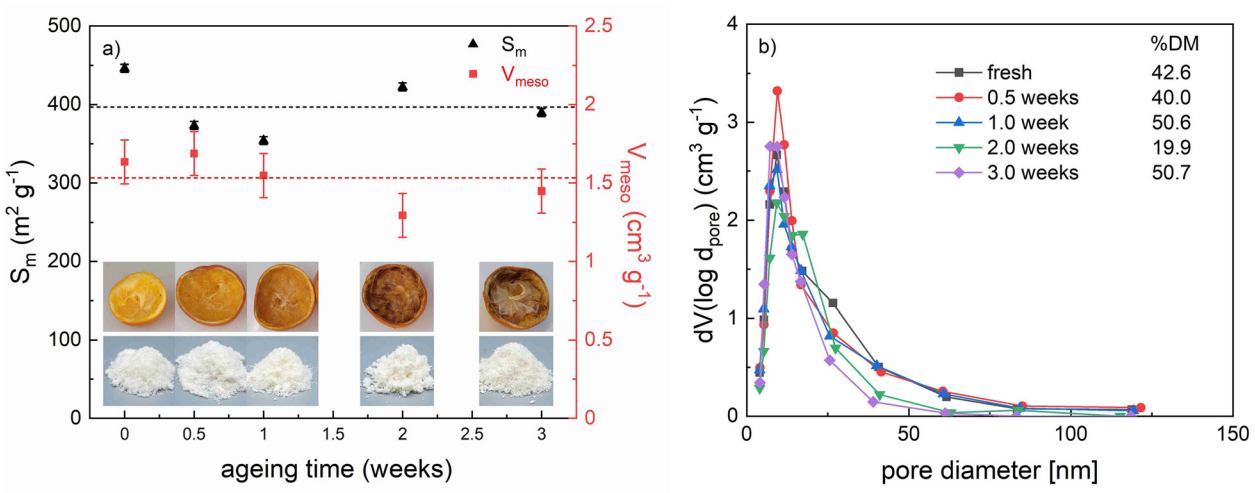

Fig. 7 (a) Specific surface areas (black) and mesopore volumes (red) of aerogels made from waste generated during orange juice production, shown as a function of storage time. Error bars correspond to the estimated standard error of the methods; dashed lines highlight the average values. The images (inset) show the sample appearances after different storage times (top) and after the conversion to the corresponding aerogel powder (bottom). (b) Pore size distributions and %DM values of the samples.

after three weeks, a significant increase in the %DM was observed. We surmise that further conversion (including depolymerization and desertification) of some pectin fractions between two and three weeks storage time led to an increased water solubility and loss of these fractions due to out washing. The remaining pectin in the solid aerogel backbone (detected after three weeks) was then a high %DM fraction. In summary, our results suggested that no severe changes of the aerogel microstructure happened due to storage, but the composition (and therefore chemical functionality) was altered. Microbial and enzymatic induced processes led to changes in chemical functionality, particularly affecting the pectin fraction. We'd like to emphasize that the showcased example represents a single case and cannot be directly applied to other samples, as each requires individual analysis.

It must also be noted that the upcycling of food residues as raw materials for the production of bioaerogels intended as food ingredients requires the waste material to comply with stringent hygienic and quality requisites. In particular, food raw materials cannot be deteriorated but freshly transformed through the application of food-grade procedures. This would of course require a change in the actual food waste management practices, involving the set-up of dedicated lines for waste collection, pretreatment and final bioaerogel production. It can be affirmed that the main hazard found in fresh fruit and vegetable waste is microbial growth, due to the perishable nature of this biomass. It is – however – worth mentioning that solvent exchange with ethanol, which is necessary for bioaerogel production, offers an easy step of stabilization of the waste from a microbiological point of view, whose antimicrobial effects are further supported by the subsequent supercritical-CO_2-drying.[83] Additionally, the extraction of decomposition products during aerogel-processing is expected. This was evident in our case, as all final aerogel samples were nearly color and odorless, despite significant microbiological activity (including mold growth) occurring after approximately two weeks storage time (Fig. 7a).

3.3 Environmental assessment

In this section, we compare the process presented in this work with a conventional sol–gel aerogel fabrication method, focusing on their environmental friendliness. So far, numerous methods for environmental assessment have been developed. In this work, we adopt the environmental assessment methodology and the approach proposed by Biwer and Heinzle[84,85] to identify the environmental "hot spots" of the process. It is important to emphasize that our analysis focuses solely on the process itself and does not evaluate whether producing a given product is reasonable or sustainable. To benchmark our approach, we compare our process with an archetypal sol–gel cellulose aerogel fabrication process reported by Cai *et al.*[86]

In the conventional process, microcrystalline cellulose is dissolved in an aqueous solution of sodium hydroxide and urea. The cellulose is then regenerated into a gel form by casting it into a regeneration bath containing diluted sulfuric acid. The resulting hydrogel is washed with deionized water, followed by solvent exchange with ethanol and drying using supercritical CO_2. The process parameters and assumptions for both the conventional and our novel processes are detailed in the ESI (Tables S4–S8†). Briefly, we first establish a material balance for both the conventional and novel processes. Based on this material balance, we calculate the Mass Index (MI) for all input and output components.[87] For input materials, the MI represents the amount of a given component consumed to produce a unit mass of the final product (all calculations are standardized to 1 g of aerogel). For output components, the MI indicates the quantity of a component generated and subsequently disposed of per unit mass of the final product.

The environmental impact of each compound involved in the process is assessed across 15 impact categories (ICs), including land use, acute toxicity, and global warming potential, among others. Each component is assigned to one of three relevance classes (A, B, or C) within each category, corresponding to high, moderate, and low relevance, respectively (see assignment in ESI, Tables S4–8†). These ICs are further grouped into six impact groups, each representing key environmental, health, or safety concerns. In the next step, numerical values are assigned to classes A, B, and C, allowing us to derive an environmental factor (EF) for each component based on its classification within the impact groups. The final environmental impact is then determined by multiplying each component's MI by its EF, yielding the Environmental Index (EI).

This index helps identify the most environmentally significant components in the process. We computed the EI for both the conventional (Fig. 8a) and novel (Fig. 8b) processes, considering all input and output components. The analysis clearly demonstrates that ethanol and carbon dioxide are the two most environmentally impactful substances in both processes, primarily due to their use in the final solvent exchange and supercritical drying steps. These compounds contribute the most to the overall environmental indices. Notably, integrated process designs have been proposed to reduce their consumption.[88,89] Moreover, their environmental impact is significantly lower at the industrial scale, where both ethanol and CO_2 can be recovered and reused in a closed-loop system (annotated with "rec." in Fig. 8). This highlights the importance of process optimization and scale-up strategies in aerogel production in order to minimize environmental burdens. The total sum of all EIs (both input and output) represents the EI of the entire process and provides an overall measure of its environmental impact. Our results indicate that the process developed in this work (EI = 28 index points per gram of aerogel) is significantly more environmentally favorable than the conventional sol–gel regeneration process (EI = 57). Notably, the material intensity of both processes is comparable (669.8 g g^{-1} aerogel *vs.* 740.1 g g^{-1} aerogel, respectively). Furthermore, our process does not involve any chemicals beyond ethanol and carbon dioxide, whereas the conventional sol–gel process relies on NaOH/urea solutions and an acidic regeneration bath. In conclusion, the tissue-based approach provides a more environmentally sustainable alternative to conventional biopolymer aerogel fabrication while

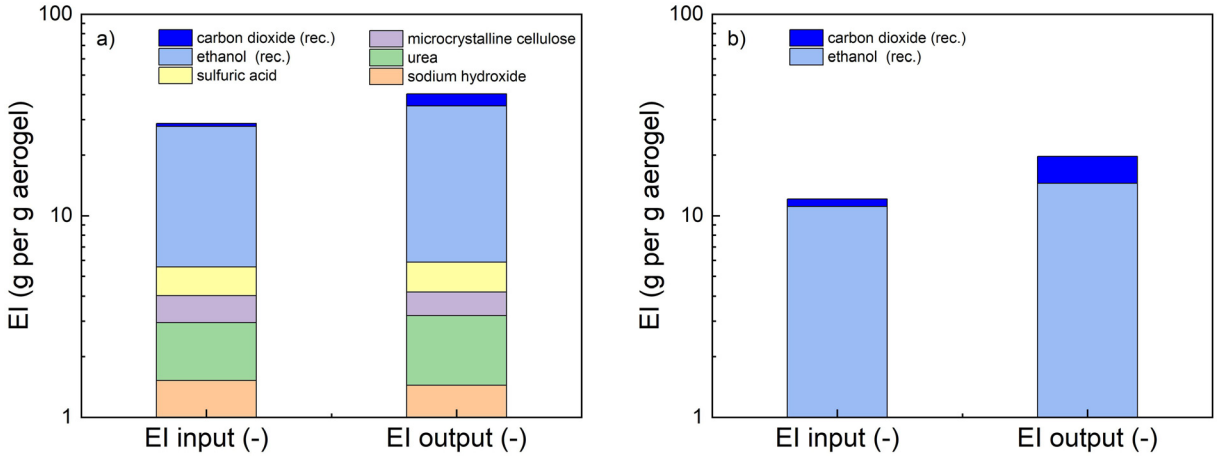

Fig. 8 Comparison of Environmental Indices (EIs) of the input and output for a conventional sol–gel (a) and the process reported in this work (b). Note log-scale on the *y*-axis.

maintaining comparable material efficiency. Our process eliminates the need for strong acids and bases and significantly reduces its overall environmental impact. While the comparison in this section was based on a specific example, the findings are likely relevant to other sol–gel or nanofiber-based methods, which generally require additional chemicals beyond ethanol and CO_2. This highlights the potential of the tissue-based approach as a promising and sustainable alternative for aerogel production.

3.4 Use of supercritically dried tissues in oleogelation

The oil structuring capacity and use of various tissue-derived aerogels as oleogel templates are evaluated in this section. To this aim, among aerogels shown in Fig. 2, those obtained from orange (pulp and peel), banana peel, kiwi, radish, nectarine and mushroom were selected. This selection was based on (a) microstructural, (b) compositional and (c) source related aspects. Samples with max. specific surface area (kiwi and radish) were chosen from different microstructural categories with mainly small (category 1) and large (category 3) mesopores. Additional examples from category 3 (nectarine and orange samples) represent samples with lower mesopore volume and specific surface area than the kiwi aerogels. Peels were included to assess the use of classical food waste/inedible parts as functional food ingredients. The mushroom sample is representative for a different biopolymer composition (highest protein content and presence of chitin). The selected aerogels were added with increasing amounts of sunflower oil: corresponding gradual changes in appearance are exemplary shown for the orange pulp sample in the main text (Table 2), for all other samples we refer to Fig. S8 and S9.†

Upon the initial addition of oil, all samples displayed a granular morphology, characterized by the formation of small aggregates. In these aerogel–oil mixtures, capillary forces promoted oil absorption into the aerogel pores, with minimal surface interaction among the aerogel particles.[90] As the oil content increased, it progressively interacted with the hydrophobic groups present on the surface of the aerogel particles, forming oil bridges between them (Table 2 and Fig. S8, S9†). Concomitantly, hydrophilic interactions among the aerogel particles in a lipophilic environment contributed to the formation of a continuous particle network.[91] By further increasing the oil amount, particle dilution in the oil reduced surface particle–particle interactions, thereby weakening the particle network and resulting in a fluid system. This behavior aligns with observations reported in previous studies relevant to oil structuring using sol–gel-based protein aerogels.[47] Based on the results, a minimum oil content oil_{gel} could be identified, at which the transition from a granular solid to a continuous self-standing oleogel occurred (Table 2 and Fig. S8 and S9†) and was chosen for further comparison of oleogel performances. The appearance of the obtained oleogels, along with their physical and rheological properties, is summarized in

Table 2 Images of orange-pulp based aerogel particles mixed with increasing amounts of sunflower oil. % is given as w/w oil aerogel

Oil uptake [%]	83.3%	90.9%	93.9% = oil_{gel}	95.2%	96.2%
Appearance			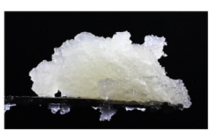	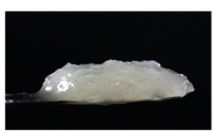	

Table 3. The minimum oil content necessary to form oleogels depended on the nature of the aerogel-matrix, varying in the range of high values from oil_{gel} = 89–99% (Table 3). These values are significantly higher than those formerly reported for sol–gel-based aerogels derived from both whey and potato proteins (70–84%).[47,50,55]

By contrast, the high oil absorption capacities are in agreement with those relevant to tissue-aerogels prepared from lettuce leaves without previous grinding.[45] In that case, the high oil absorption capacity was attributed to the peculiar response of plant tissues to the aerogel production process, which was demonstrated to lead to an expansion of the cellular structure, possibly enhancing the volume available for oil uptake.[43] It is noteworthy that in the present work, plant tissues were finely ground, causing a loss of cell integrity with the release of compartmentalized cellular content (Fig. 4). Upon oil absorption, fractions of cell walls and thylakoids (in fluorescence) dispersed in oil (in yellow) were clearly evident, with morphologies depending on the initial vegetable material, in the confocal micrographs of oleogels (Fig. 9 and Fig. S10†). It can be observed that these cellular fractions, which appeared tightly packed in the mesoporous aerogel structure (see Fig. 4 and Fig. S6†), tended to expand, detaching one from the other and begetting large spaces holding oil among them. In other words, the aerogel particles likely swelled upon absorbing oil, which probably expanded the fibrous matrix and exposed functional groups.

Among these, hydrophobic groups present in proteins, which were shown to be still present in the aerogel matrix (see Table S2†), could play a not negligible role in driving interactions of aerogels with oil. Aerogel swelling was also observed for the mushroom based sample: however, since mushrooms do not present a cellular structure analogous to fruits and vegetables, they beget oleogels formed by fine stranded fibers homogeneously distributed in the oleogel network. As shown in Table 3, the oleogel oil content depended on the original vegetable material. In detail, radish led to the oleogel with the highest oil content, followed by mushroom, kiwi, nectarine, orange, banana peel, and orange peel. Unlike sol–gel-based, pure protein aerogels,[47,50,55] no direct significant correlation between oil absorption and microstructural features (surface area and mesoporous volume) was observed ($p > 0.05$), suggesting that oil absorption could be driven not only by microstructural properties but also by compositional factors in our case. No relationship with the pectin content was identified, which aligns with the low %DM values found in our samples, which indicated a rather weak interaction of the pectin fraction with oil. An interesting correlation ($R = 0.92$, $p < 0.05$) was found between oil absorption and the reciprocal of the product of the protein content and surface area of the aerogels (Fig. 10).

Table 3 Appearance, oil holding capacity (OHC), elastic modulus (G'), and loss tangent (tan δ), and microstructure of oleogels prepared from different tissue-derived aerogels and containing the minimum oil amount (%) leading to a continuous structure

Tissue	oil_{gel} (%)	Appearance	OHC (%)	G' (10^4 Pa)	Tan δ
Orange peel	88.9		97.1 ± 0.7	25.4 ± 4.3	0.043 ± 0.010
Orange	93.8		90.5 ± 1.8	6.1 ± 0.5	0.076 ± 0.007
Banana peel	93.8	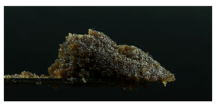	91.6 ± 0.8	6.5 ± 0.5	0.054 ± 0.001
Kiwi	96.1	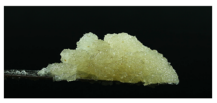	91.7 ± 3.2	5.1 ± 0.2	0.057 ± 0.002
Radish	98.7	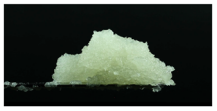	91.6 ± 0.8	1.2 ± 0.1	0.057 ± 0.002
Nectarine	95.2	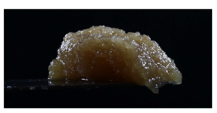	93.8 ± 1.3	5.8 ± 3.1	0.073 ± 0.005
Mushroom	96.0	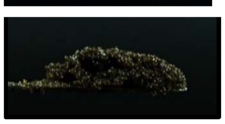	97.2 ± 1.1	2.6 ± 0.3	0.066 ± 0.003

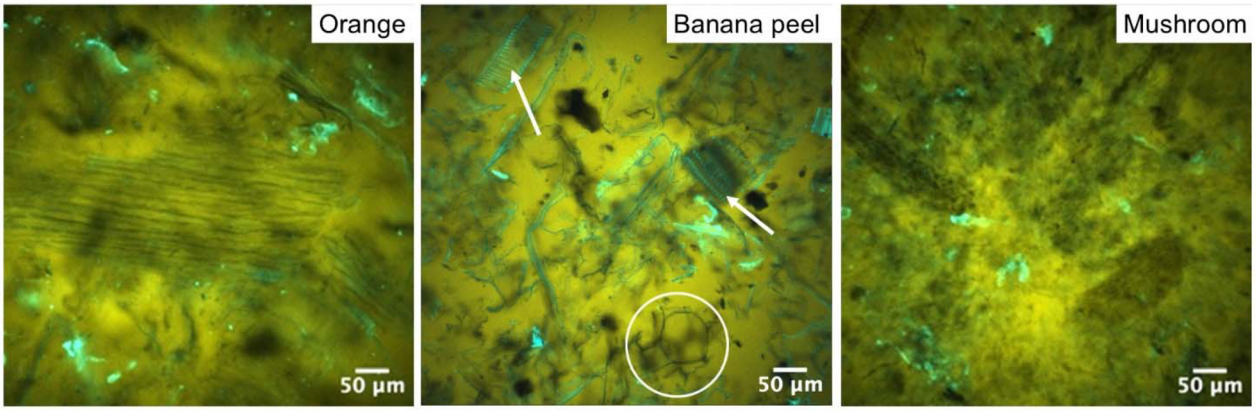

Fig. 9 Confocal micrographs of oleogels based on different tissue-based aerogels. Highlighted areas in the middle image: white circle = detached cell walls, white arrows = closely spaced xylem fibers.

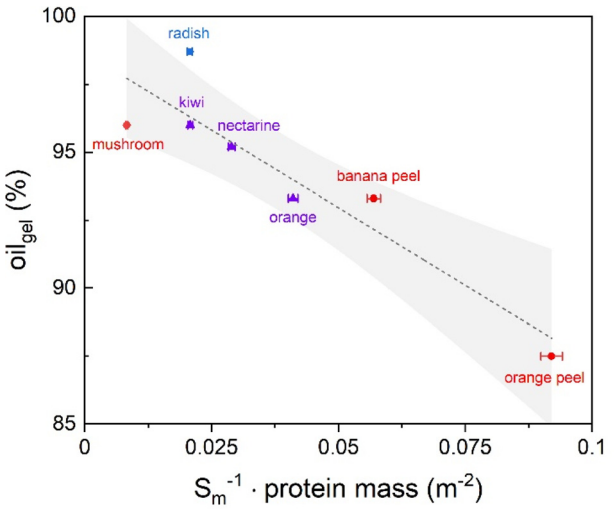

Fig. 10 Correlation of oil absorption of tissue-based aerogels with the reciprocal of the product of protein content and surface area. X-errors represent the standard error of BET measurements; the straight line corresponds to linear fitting and the hatched area to the 95% confidence interval. The color/symbol code is according to aerogel categories as defined in section 3.1 (see Fig. 3).

This relationship might suggest that oil absorption increases synergically with the availability of surfaces exposing hydrophobic groups, reasonably derived from proteins. Throughout the samples with the highest oil absorption capability, the mushroom aerogel contains the by far highest protein content (~43%), while the radish aerogel presents an elevated internal surface area combined with a still significant protein amount (~15%) as compared to most other samples, leading most probably to the maximum oil uptake observed in this work. The combination of proteins, acting as surface active materials, with the representative high-content pectin polysaccharides, can provide stable steric repulsions: therefore, the high amount of protein covalently bound to a highly branched polysaccharide structure represented by the unique content of rhamnose from the radish sample may result in particularly beneficial surface–oil interactions.[92] As regards the OHC, all samples exceeded 90%, demonstrating that the oil was strongly retained in the aerogel structure in all cases (Table 3). From a rheological point of view, the obtained oleogels exhibited typical gel-like rheological profiles, characterized by a storage modulus (G') higher than the loss modulus (G'') in the linear viscoelastic region (LVR) (Table 3). The yield resistance and elastic properties of the oleogels were attributed to the network formed by aerogel particles in the oil, resulting in a plastic and deformable structure. Moreover, for all the oleogels, the frequency sweep test showed the independence of G' and G'' in the frequency range considered, suggesting the strong gel behavior of the samples. Likewise, the low loss tangent ($\tan\delta$) value, approaching zero, indicated that the elastic (solid-like) behavior of the material dominated over its viscous (liquid-like) modulus. These results are in agreement with the rheological properties of oleogels obtained from sol–gel-based aerogel particles.[50,55] It must be underlined how the rheological parameters of the oleogels were comparable to those of commercial hard fat (*e.g.*, butter, palm oil, margarine, laminating shortening)[93] making these materials ideal fat-replacers in real-food matrixes, while requiring only small amounts of aerogel regarding the overall oil mass (down to 1% in the case of radish aerogels).

4 Conclusion

In this study, we demonstrated for the first time that the inherent porosity of various natural tissues – which have not yet been utilized as aerogels – can be directly harnessed to convert them into biopolymer aerogels. Unlike sol–gel or nanofiber-based aerogel production, our approach eliminates the need for biopolymer extraction, dissolution, gelation, and additional additives. This streamlines the production process, making aerogel manufacturing more environmentally friendly and sustainable. Our key finding is that tissue based aerogels

exhibit textural properties comparable to many single-component materials obtained *via* sol–gel processes. The materials presented high specific surface areas, with a maximum of up to ~446 m^2 g^{-1} (in the case of orange residues obtained after juice production). These results underscore the potential of food waste as a valuable porous high-performance material. The specific use case in this study was the application of tissue based aerogels as oleogel-templates: our results showed that our materials can transform liquid oils into oleogels with rheological properties similar to solid fats, achieving exceptionally high efficiency (oil uptake of up to ~99%) and excellent oil retention (91–97%).

For dissemination, our project can leverage open public science *via* the aerogel.kniffelix.de platform: for access to the interactive learning platform, we refer to aerogel.kniffelix.de and for download of learning materials to aerogel-download-material.kniffelix.de, where experiments are accessible to the public and can be carried out in part using common household materials. This open access STEM resource will support engagement through educational videos and hands-on aerogel experiments, promoting both scientific literacy and community engagement in sustainable materials science. Overall, this study highlights the feasibility of utilizing food industry by-products, such as fruit and vegetable tissues, as sources of valuable aerogel products, aligning with sustainable development goals by contributing to the reduction and valorization of food waste through innovative, environmentally friendly technological applications. We suggest that the fundamental idea behind this study – seeing all kinds of organic tissues as naturally grown hydrogels – is extendable to a huge variety of other sources and hope our results promote the further exploration of the direct tissue-to-aerogel route.

Author contributions

The manuscript was written through contributions of all authors. All authors have given approval to the final version of the manuscript.

Human and animal rights

This manuscript does not contain any studies with human participants or animals performed by any of the authors.

Data availability

The data supporting this article have been included as part of the ESI.†

Conflicts of interest

All authors declare that they have no conflict of interest.

Acknowledgements

The authors wish to acknowledge support for this research received from the Bundesministerium für Bildung und Forschung (BMBF) within the framework of the "Dahrendorf-project for the EU project NanoHybrids", funding code 01DT22001.

This work was carried out in the frame of the COST Action CA18125 "Advanced Engineering and Research of aeroGels for Environment and Life Sciences" (AERoGELS) and funded by the European Commission.

The Accreditation as Center of Excellence Severo Ochoa IATA-CSIC, CEX2021–001189-S funded by MCIU/AEI/10.13039/501100011033 is also fully acknowledged.

References

1 S. Kaza, L. Yao, P. Bhada-Tata and F. Van Woerden, *What a Waste 2.0 - A Global Snapshot of Solid Waste Management to 2050*, World Bank Publications, Washington, DC, 2018.
2 United Nations Environment Programme, Food Waste Index Report 2024. Think Eat Save: Tracking Progress to Halve Global Food Waste, UNEP, Nairobi, 2024.
3 S. P. Sha, D. Modak, S. Sarkar, S. K. Roy, S. P. Sah, K. Ghatani and S. Bhattacharjee, *Front. Microbiol.*, 2023, **14**, 1260071.
4 A. Alammar, R. Hardian and G. Szekely, *Green Chem.*, 2022, **24**(1), 365–374.
5 H. Liu, T. Wang, J. Wang, G. Gao, Y. Li and D. Ren, *Green Chem.*, 2025, **27**, 1125–1144.
6 C. Y. Cheok, N. Mohd Adzahan, R. Abdul Rahman, N. H. Zainal Abedin, N. Hussain, R. Sulaiman and G. H. Chong, *Crit. Rev. Food Sci. Nutr.*, 2018, **58**, 335–361.
7 T. Ahmad, F. A. Masoodi, S. A. Rather, S. M. Wani and A. Gull, *J. Biol Chem. Chron.*, 2019, **5**(1), 114–122.
8 S. R. R. Comim, K. Madella, J. V. Oliveira and S. R. S. Ferreira, *J. Supercrit. Fluids*, 2010, **54**(1), 30–37.
9 D. San Martin, S. Ramos and J. Zufía, Valorisation of Food Waste to Produce New Raw Materials for Animal Feed, *Food Chem.*, 2016, **198**, 68–74.
10 C. H. Tan, C. L. Hii, C. Borompichaichartkul, P. Phumsombat, I. Kong and L. P. Pui, *Drying Technol.*, 2022, **40**(8), 1514–1538.
11 M. Vetralla, G. Ferrentino, A. Zambon and S. Spilimbergo, *ETP Int. J. Food Eng.*, 2018, **4**(3), 186–190.
12 A. Zambon, S. Bourdoux, M. F. Pantano, N. M. Pugno, F. Boldrin, G. Hofland, A. Rajkovic, F. Devlieghere and S. Spilimbergo, *Drying Technol.*, 2021, **39**(2), 259–267.
13 A. Zambon, P. Facco, G. Morbiato, M. Toffoletto, G. Poloniato, S. Sut, P. Andrigo, S. Dall'Acqua, M. De Bernard and S. Spilimbergo, *Food Chem.*, 2022, **397**, 133789.
14 K. Pravallika, S. Chakraborty and R. S. Singhal, *J. Food Eng.*, 2023, **343**, 111375.
15 T. Budtova, *Cellulose*, 2019, **26**(1), 81–121.

16 S. Zhao, W. J. Malfait, N. Guerrero-Alburquerque, M. M. Koebel and G. Nyström, *Angew. Chem., Int. Ed.*, 2018, **57**(26), 7580–7608.
17 R. Subrahmanyam, P. Gurikov, P. Dieringer, M. Sun and I. Smirnova, *Gels*, 2015, **1**(2), 291–313.
18 *Springer Handbook of Aerogels*, ed. M. A. Aegerter, N. Leventis, M. Koebel and S. A. Steiner III, Springer Handbooks; Springer International Publishing, Cham, 2023.
19 K. Ganesan, T. Budtova, L. Ratke, P. Gurikov, V. Baudron, I. Preibisch, P. Niemeyer, I. Smirnova and B. Milow, *Materials*, 2018, **11**(11), 2144.
20 F. Ciuffarin, M. Négrier, S. Plazzotta, M. Libralato, S. Calligaris, T. Budtova and L. Manzocco, *Food Hydrocolloids*, 2023, **140**, 108631.
21 V. Baudron, P. Gurikov, I. Smirnova and S. Whitehouse, *Gels*, 2019, **5**(1), 12.
22 P. T. T. Nguyen, N. H. N. Do, X. Y. Goh, C. J. Goh, R. H. Ong, P. K. Le, N. Phan-Thien and H. M. Duong, *Waste Biomass Valorization*, 2022, **13**(4), 1825–1847.
23 N. H. N. Do, T. P. Luu, Q. B. Thai, D. K. Le, N. D. Q. Chau, S. T. Nguyen, P. K. Le, N. Phan-Thien and H. M. Duong, *Mater. Technol.*, 2020, **35**(11–12), 807–814.
24 S. Chaudhary and D. T. K. Dora, *Biomass Convers. Biorefinery*, 2023.
25 P. X. T. Nguyen, K. H. Ho, C. T. X. Nguyen, N. H. N. Do, A. P. N. Pham, T. C. Do, K. A. Le and P. K. Le, *IOP Conf. Ser. Earth Environ. Sci.*, 2021, **947**(1), 012011.
26 Y. Fan, B. Lu, W. Chen, X. Zhang and X. Li, Elastic white radish-based cellulose aerogel for efficient oil-water separation, *Research Square*, 2023, preprint, DOI: **10.21203/rs.3.rs-2478285/v1**.
27 L. Manzocco, K. S. Mikkonen and C. A. García-González, *Food Struct.*, 2021, **28**, 100188.
28 Y. Jeong, R. Patel and M. Patel, *Biomimetics*, 2024, **9**(7), 397.
29 C. A. García-González, A. Iglesias-Mejuto, C. López-Iglesias, V. Santos-Rosales, I. Ardao and C. Alvarez-Lorenzo, in *Engineering of Natural Polymeric Gels and Aerogels for Multifunctional Applications*, ed. S. Thomas, B. Seantier and B. Joseph, Elsevier, 2024, ch. 5, pp 125–157.
30 I. Smirnova and P. Gurikov, *J. Supercrit. Fluids*, 2018, **134**, 228–233.
31 T. Budtova, D. A. Aguilera, S. Beluns, L. Berglund, C. Chartier, E. Espinosa, S. Gaidukovs, A. Klimek-Kopyra, A. Kmita, D. Lachowicz, F. Liebner, O. Platnieks, A. Rodríguez, L. K. Tinoco Navarro, F. Zou and S. J. Buwalda, *Polymers*, 2020, **12**(12), 2779.
32 C. S. A. Bento, B. Agostinho, A. Teixeira, M. S. Reis, H. C. De Sousa and M. E. M. Braga, *J. Supercrit. Fluids*, 2024, **211**, 106321.
33 M. Schwan, S. Nefzger, B. Zoghi, C. Oligschleger and B. Milow, *Front. Mater.*, 2021, **8**, 662487.
34 R. Subrahmanyam, I. Selmer, A. Bueno, D. Weinrich, W. Lölsberg, M. Fricke, S. Movahhed, P. Gurikov and I. Smirnova, in *Springer Handbook of Aerogels*, ed. M. A. Aegerter, N. Leventis, M. Koebel and S. A. Steiner III, Springer International Publishing, Cham, 2023, pp 93–120.
35 İ. Şahin, Y. Özbakır, Z. İnönü, Z. Ulker and C. Erkey, *Gels*, 2017, **4**(1), 3.
36 I. I. Khudeev, A. E. Lebedev, M. S. Mochalova and N. V. Menshutina, *Drying Technol.*, 2024, **42**(5), 812–835.
37 J. Cai, S. Kimura, M. Wada, S. Kuga and L. Zhang, *ChemSusChem*, 2008, **1**(1–2), 149–154.
38 O. Aaltonen and O. Jauhiainen, *Carbohydr. Polym.*, 2009, **75**(1), 125–129.
39 A. Rege, M. Schestakow, I. Karadagli, L. Ratke and M. Itskov, *Soft Matter*, 2016, **12**(34), 7079–7088.
40 A. Zaman, F. Huang, M. Jiang, W. Wei and Z. Zhou, *Energy Built Environ.*, 2020, **1**(1), 60–76.
41 B. Schroeter, V. P. Yonkova, N. A. M. Niemeyer, I. Jung, I. Preibisch, P. Gurikov and I. Smirnova, Cellulose Aerogel Particles: Control of Particle and Textural Properties in Jet Cutting Process, *Cellulose*, 2021, **28**(1), 223–239.
42 L. T. Possari, C. G. Otoni, T. Budtova and S. H. P. Bettini, Upcycling orange waste biomass into bio-aerogels, *ChemRxiv*, 2024, preprint, DOI: **10.26434/chemrxiv-2024-q8gtn**.
43 S. Plazzotta, S. Calligaris and L. Manzocco, *Innovative Food Sci. Emerging Technol.*, 2018, **47**, 485–492.
44 G. Gaggero, R. P. Subrahmanyam, B. Schroeter, P. Gurikov and M. Delucchi, *Gels*, 2022, **8**(11), 691.
45 S. Plazzotta, S. Calligaris and L. Manzocco, *LWT*, 2018, **89**, 276–283.
46 I. Selmer, C. Kleemann, U. Kulozik, S. Heinrich and I. Smirnova, Development of Egg White Protein Aerogels as New Matrix Material for Microencapsulation in Food, *J. Supercrit. Fluids*, 2015, **106**, 42–49.
47 I. Jung, B. Schroeter, S. Plazzotta, L. De Berardinis, I. Smirnova, P. Gurikov and L. Manzocco, *Food Hydrocolloids*, 2023, **142**, 108758.
48 S. Plazzotta, S. Calligaris and L. Manzocco, *J. Food Eng.*, 2023, **351**, 111522.
49 L. Manzocco, S. Plazzotta, J. Powell, A. De Vries, D. Rousseau and S. Calligaris, *Food Hydrocolloids*, 2022, **122**, 107117.
50 S. Plazzotta, I. Jung, B. Schroeter, R. P. Subrahmanyam, I. Smirnova, S. Calligaris, P. Gurikov and L. Manzocco, *Polymers*, 2021, **13**(23), 4063.
51 N. Shokri, B. Stevens, K. Madani, J. Grabe, M. Schlüter and I. Smirnova, *ACS Eng. Au*, 2023, **3**(1), 3–6.
52 L. Geuer, G. Liese, M. Roth, A. Liese, S. Perret, A. Schlindwein and R. Ulber, *Chem. Unserer Zeit*, 2024, **58**(4), 216–223.
53 G. Liese, F. Rohweder, J. Husung, L. Gibowsky, B. Schroeter, I. Smirnova and A. Liese, *Chem. Ing. Tech.*, 2022, **94**(9), 1379–1380.
54 C. Kleemann, I. Selmer, I. Smirnova and U. Kulozik, *Food Hydrocolloids*, 2018, **83**, 365–374.
55 S. Plazzotta, S. Calligaris and L. Manzocco, *Food Res. Int.*, 2020, **132**, 109099.
56 D. A. Méndez, B. Schroeter, A. Martínez-Abad, M. J. Fabra, P. Gurikov and A. P. López-Rubio, *Carbohydr. Polym.*, 2023, **306**, 120604.
57 J. F. Saeman, *Ind. Eng. Chem.*, 1945, **37**(1), 43–52.

58 M. A. Joslyn and J. D. Ponting, *Advances in Food Research*, Elsevier, 1951, 3, pp 1–44.
59 A. Hosikian, S. Lim, R. Halim and M. K. Danquah, *Int. J. Chem. Eng.*, 2010, **2010**, 1–11.
60 T. Arumugham, K. Rambabu, S. W. Hasan, P. L. Show, J. Rinklebe and F. Banat, *Chemosphere*, 2021, **271**, 129525.
61 J. Martínez and A. Aguiar, *Curr. Anal. Chem.*, 2013, **10**(1), 67–77.
62 E. Reverchon, *J. Supercrit. Fluids*, 1997, **10**(1), 1–37.
63 N. A. M. Eskin and E. Hoehn, in *Biochemistry of Foods*, Elsevier, 2013, ch. 2, pp 49–126.
64 D. A. Brummell, *Funct. Plant Biol.*, 2006, **33**(2), 103.
65 M. Becker, K. Ahn, M. Bacher, C. Xu, A. Sundberg, S. Willför, T. Rosenau and A. Potthast, *Cellulose*, 2021, **28**(13), 8719–8734.
66 S. Levigne, M. Thomas, M.-C. Ralet, B. Quemener and J.-F. Thibault, Determination of the Degrees of Methylation and Acetylation of Pectins Using a C18 Column and Internal Stand-ards, *Food Hydrocolloids*, 2002, **16**(6), 547–550, DOI: 10.1016/S0268-005X(02)00015-2.
67 J. S. J. Santiago, C. Kyomugasho, S. Maheshwari, Z. Jamsazzadeh Kermani, D. Van De Walle, A. M. Van Loey, K. Dewettinck and M. E. Hendrick, *Food Hydrocolloids*, 2018, **77**, 482–493.
68 E. L. La Cava, E. Gerbino, S. C. Sgroppo and A. Gómez-Zavaglia, *J. Food Sci.*, 2018, **83**(6), 1613–1621.
69 A. G. J. Voragen, G.-J. Coenen, R. P. Verhoef and H. A. Schols, *Struct. Chem.*, 2009, **20**(2), 263–275.
70 H. M. Ng, N. M. Saidi, F. S. Omar, K. Ramesh, S. Ramesh and S. Bashir, *Encyclopedia of Polymer Science and Technology*, Wiley, 2018, pp. 1–29, DOI: 10.1002/0471440264.pst667.
71 M. Thommes, K. Kaneko, A. V. Neimark, J. P. Olivier, F. Rodriguez-Reinoso, J. Rouquerol and K. S. W. Sing, *Pure Appl. Chem.*, 2015, **87**(9–10), 1051–1069.
72 G. Horvat, M. Pantić, Ž. Knez and Z. Novak, *Gels*, 2022, **8**(7), 438.
73 A. Veronovski, G. Tkalec, Ž. Knez and Z. Novak, *Carbohydr. Polym.*, 2014, **113**, 272–278.
74 M. Pantić, G. Horvat, Ž. Knez and Z. Novak, *Molecules*, 2020, **25**(5), 1187.
75 C. Rudaz, R. Courson, L. Bonnet, S. Calas-Etienne, H. Sallée and T. Budtova, *Biomacromolecules*, 2014, **15**(6), 2188–2195.
76 B. Schroeter, I. Jung, K. Bauer, P. Gurikov and I. Smirnova, *Polymers*, 2021, **13**(17), 3000.
77 D. J. Andlinger, A. C. Bornkeßel, I. Jung, B. Schroeter, I. Smirnova and U. Kulozik, *Food Hydrocolloids*, 2021, **112**, 106305.
78 S. Posé, C. Paniagua, A. J. Matas, A. P. Gunning, V. J. Morris, M. A. Quesada and J. A. Mercado, *Trends Food Sci. Technol.*, 2019, **87**, 47–58.
79 W. S. Peters, K. H. Jensen, H. A. Stone and M. Knoblauch, *J. Plant Physiol.*, 2021, **257**, 153341.
80 A. W. Robards, *Nature*, 1968, **218**(5143), 784–784.
81 S. Groult and T. Budtova, *Carbohydr. Polym.*, 2018, **196**, 73–81.
82 S. Groult and T. Budtova, *Eur. Polym. J.*, 2018, **108**, 250–261.
83 A. Zambon, F. Michelino, S. Bourdoux, F. Devlieghere, S. Sut, S. Dall'Acqua, A. Rajkovic and S. Spilimbergo, *Drying Technol.*, 2018, **36**(16), 2016–2021.
84 E. Heinzle, A. P. Biwer and C. L. Cooney, *Development of Sustainable Bioprocesses: Modeling and Assessment*, Wiley, 2006, DOI: 10.1002/9780470058916.
85 A. Biwer and E. Heinzle, *J. Chem. Technol. Biotechnol.*, 2004, **79**(6), 597–609.
86 J. Cai, S. Kimura, M. Wada, S. Kuga and L. Zhang, *ChemSusChem*, 2008, **1**(1–2), 149–154.
87 E. Heinzle, D. Weirich, F. Brogli, V. H. Hoffmann, G. Koller, M. A. Verduyn and K. Hungerbühler, *Ind. Eng. Chem. Res.*, 1998, **37**, 3395–3407.
88 R. Subrahmanyam, P. Gurikov, I. Meissner and I. Smirnova, *J. Visualized Exp.*, 2016, **113**.
89 A. Lebedev, E. Suslova, A. Troyankin and D. Lovskaya, *Gels*, 2021, **7**(1), 4.
90 I. Selmer, J. Karnetzke, C. Kleemann, M. Lehtonen, K. S. Mikkonen, U. Kulozik and I. Smirnova, *J. Food Eng.*, 2019, **260**, 1–11.
91 A. De Vries, Y. L. Gomez, E. Van Der Linden and E. Scholten, *RSC Adv.*, 2017, **7**(19), 11803–11812.
92 D. A. Mendez, M. J. Fabra, A. Martínez-Abad, M. Martínez-Sanz, M. Gorria and A. López-Rubio, *Food Hydrocolloids*, 2021, **120**, 106957.
93 A. I. Blake and A. G. Marangoni, Factors Affecting the Rheological Properties of a Structured Cellular Solid Used as a Fat Mimetic, *Food Res. Int.*, 2015, **74**, 284–293.